Response of an aluminium Schwarz triply periodic minimal surface lattice structure under constant amplitude and random fatigue

Matteo Gavazzoni, Stefano Beretta, Stefano Foletti

This is a post-peer-review, pre-copyedit version of an article published in *International Journal of Fatigue*. The final authenticated version is available online at:
https://doi.org/10.1016/j.ijfatigue.2022.107020

DIPARTIMENTO DI MECCANICA ■ POLITECNICO DI MILANO
via G. La Masa, 1 ■ 20156 Milano ■ EMAIL (PEC): pecmecc@cert.polimi.it
http://www.mecc.polimi.it
Rev. 0

Journal Pre-proof

Response of an aluminium Schwarz triply periodic minimal surface lattice structure under constant amplitude and random fatigue

Matteo Gavazzoni, Stefano Beretta, Stefano Foletti

PII: S0142-1123(22)00285-7
DOI: https://doi.org/10.1016/j.ijfatigue.2022.107020
Reference: JIJF 107020

To appear in: *International Journal of Fatigue*

Received date : 19 January 2022
Revised date : 16 May 2022
Accepted date : 18 May 2022

Please cite this article as: M. Gavazzoni, S. Beretta and S. Foletti, Response of an aluminium Schwarz triply periodic minimal surface lattice structure under constant amplitude and random fatigue. *International Journal of Fatigue* (2022), doi: https://doi.org/10.1016/j.ijfatigue.2022.107020.

Response of an aluminium Schwarz triply periodic minimal surface lattice structure under constant amplitude and random fatigue

Matteo Gavazzoni, Stefano Beretta, Stefano Foletti*

Dipartimento di Meccanica, Politecnico di Milano
Via La Masa 1, Milano I-20156, Italy

Abstract

This paper presents an investigation about fatigue behaviour of an aluminium triply periodic minimal surface lattice structures, printed with Selective Laser Melting. Aim of the paper is to experimentally characterize constant and variable amplitude fatigue strength and to assess if current methodologies for predicting random fatigue strength of solid materials can be extended also to lattice structures, in a homogenized setting. The investigation is complemented by a detailed analysis of samples fracture surface, corroborated by numerical analyses, and a comprehensive discussion on the evolution of the damage observed in the experiments.

Research highlights

- Fatigue strength of a TPMS lattice structure manufactures in AlSi10Mg by L-PBF
- Constant amplitude fatigue characterization at different stress ratios
- Random fatigue characterization at different RMS levels
- Detailed characterization of the failure mechanisms
- Fatigue life under variable amplitude well predicted by the Miner's rule

Keywords: Advanced materials, Lattice structures, Damage accumulation, Random fatigue

1. Introduction

Lattice structures are architected materials constituted by the periodic repetition of a unit cell in the space, heterogeneous at the micro-scale. They can be treated as meta-materials at the macro-scale and offer the possibility to obtain peculiar combination of physical properties that cannot be obtained with solid materials. Their effective properties (thermal, optical, mechanical...) depends on three main factors: cell topology, relative density and base material [1]. Depending on the type of topology, lattice structures can be subdivided into two classes: strut-based and sheet-based lattices. In the former, the unit cell is composed by struts connected at the nodes [2–4] while, in the

*Corresponding author
Email address: stafano.foletti@polimi.it (Stefano Foletti)

latter, the unit cell is composed by thin walls [5, 6]. Among sheet-based lattices, Triply Periodic Minimal Surface (TPMS) structures have attracted particularly the interest of researchers in the last few years. TPMS structures are obtained by non-self intersecting surfaces with zero mean curvature that can be described by mathematical equations [7–11] and partition the volume in two distinct and not communicating sub-volumes.

The recent improvements in metal 3D printing techniques and their consequent commercial diffusion have increasingly shifted the focus to metallic lattices, that were successfully implemented in a broad range of application fields [12]. For example, the possibility to parallel the values of elastic modulus of human bone, as well as the good permeability and the high porosity make titanium TPMS lattices distinctly suitable for biomedical implants [9, 11, 13, 14]. Furthermore, the presence of two not communicating sub-volumes with smooth boundaries and the high thermal conductivity offer the possibility to implement metallic (in particular aluminium) TPMS lattices in fluid heat exchangers, feed spacers and catalytic supports [15–19], with a significant improvement in their performances.

The prediction of macroscopic (or effective) mechanical response of metallic lattices, as well as assessment procedures for structural integrity are crucial to successfully exploit the advantages they offer. Although the static behaviour of metallic lattices is a fully-addressed topic in literature, there are still open points concerning fatigue strength [20]. Most of the works present in literature about experimental fatigue characterization of metallic lattices investigate compression-compression fatigue, given the lower complexity of the experimental set-up [21–24]. These works show that fatigue properties of lattice structures are strongly dependent on the topology of the unit cell. It was found that TPMS structures generally outperform strut based lattices, as they do not display significant geometrical singularity: for strut based lattices, the presence of nodes leads to stress concentrations, acting as cracks triggers and lowering the fatigue strength [9, 20, 24]. Other works showed that manufacturing defects can strongly influence the fatigue resistance of lattices obtained by additive manufacturing [25–29], similarly to AM bulk metals, which static and fatigue properties might be significantly different from those of materials obtained by conventional processes. It is well known that the fatigue behaviour of AM metals is affected by the presence of manufacturing defects and microstructural inhomogeneities [30–33], which in turns depend on the thermal history of the material, the building direction, the powder characteristics and the process parameters. Given the small dimension of lattice structure constitutive elements (struts or walls, depending on the topology), the effect of surface features is more pronounced than the one of internal defects [28, 34, 35]. However, the use of classical literature tools, such as the Kitagawa-Takahashi diagram [36] or the critical distance theory [28], allow to correctly describe imperfections knockdown factor on their fatigue strength.

The fatigue behaviour of metallic lattices under loading conditions different from compression-compression has been studied to a lesser extent. Only a limited number of works addressing this issue for strut based lattices can be found [37–39], showing that the effect of stress ratio on the fatigue limit is different from base material behaviour and generally observing a lower sensitivity to mean stress. However, a comprehensive understanding about the influence of the stress ratio on the fatigue strength of TPMS structures and their fatigue failure mechanisms is still missing. Furthermore, industrial and commercial components are often subjected to variable loading conditions. For example, the load acting on a biomedical implant during service is far from being at constant amplitude [40–42], while aero and aerospace components are generally subjected to random vibrations during operating mission [43]. The fatigue strength of metallic lattices under variable amplitude loading has not been investigated in literature

and still represents another important open topic for many practical applications [20].

This paper addresses the constant amplitude and random fatigue strength of an aluminium Schwarz primitive TPMS lattice structure fabricated with selective laser melting (SLM). The paper has two main aims: (i) to characterize the effect of the stress ratio on the fatigue strength and on the failure mechanisms of a TPMS lattice structure and (ii) to propose a method for life prediction under variable amplitude loading conditions. A detailed experimental characterization of constant amplitude fatigue strength is performed and the effect of the mean stress is investigated, both on the fatigue strength and on the failure mechanism. The failure mechanisms analyses carried out on samples fractographies are corroborated by numerical analyses, performed with the local stress approach proposed in [28]. Random fatigue tests are carried out and the results are analysed with the Miner's rule, exploiting the results of constant amplitude characterization, to obtain the damage index [44]. We found that classical procedures are well applicable for random fatigue life of our lattice structure, observing that the experimental dispersion of the damage variable is comparable to the dispersion of the fatigue diagram. The paper is structured as follows. In Section 2, the experimental results are reported, and a detailed analyses of the failure mechanisms and fracture surfaces is provided. Constant amplitude tests results are then analysed in Section 3, while random fatigue tests are analysed in Section 4. The obtained remarks are discussed in Section 5 and Section 6 outlines the outcomes of the work.

2. Experiments

2.1. Base material, unit cell and specimen geometry

The lattice structure selected for this work is a Schwarz primitive (Figure 1a) with a unit cell size of 4 mm. The minimum thickness of the cell walls is approximately 0.24 mm, giving an as-designed relative density of 22%. Figure 1b shows the geometry of the specimens used for the experiments. The specimen has a cross section of 5x5 cells, a gauge section of 9 cells at the designed density and three additional cells per side with graded density to smooth the transition from the structure to the grips. The grips are designed so as to make possible the application of both tension and compression loads. The base material is the aluminium alloy AlSi10Mg, whose main static properties are listed in Table 1 [45]. Specimens were printed with the vertical axis aligned with the building direction, by means of Selective Laser Melting with a SLM-Solutions (Lubeck, Germany) 280 v1.0 printer, with a laser power of 350 W and scanning speed of 1150 mm/s. The layer thickness was set to 50 μm and the hatching distance to 0.17 mm. Process parameters were optimized for printing surface-based lattices. The static properties of the lattice structures obtained from tensile tests performed on this specimen geometry are reported in Table 1.

Table 1 – Static properties of AlSi10Mg base material [45] and Schwarz primitive lattice structures (relative density 22%): elastic modulus E, yielding limit σ_y, ultimate tensile strength UTS and strain at failure ε_f

	E [MPa]	σ_y [MPa]	UTS [MPa]	ε_f [%]
Base material	68000	220	410	6.20
Schwarz primitive lattice	3820	18.1	29.0	2.42

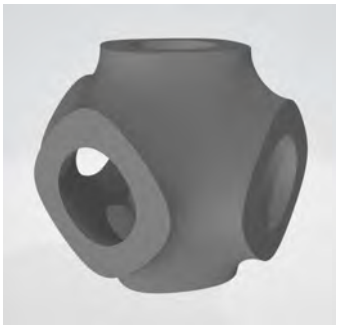

Unit cell size	4 mm
Minimum wall thickness	0.24 mm
Relative density	22%

(a)

(b)

Figure 1 – (a) Unit cell topology (Schwarz primitive TPMS) and geometrical parameters, (b) geometry of specimens used for static and fatigue experimental tests

2.2. Constant amplitude fatigue tests

The aim of fatigue characterization at constant amplitude is twofold. Firstly, to set the reference life curve (S-N curve) and to model the effect of the mean stress on the fatigue life for the analysis of random tests results. Secondly, to characterize how the fatigue strength and the failure mechanisms are affected by the stress ratios. All the fatigue tests at constant amplitude were carried out on a 10 kN electrodynamic testing machine Instron E10000, in force control at a frequency of 35 Hz and following the pertinent standards ASTM E739 and ISO 12107 [46, 47]. The end condition for the tests was set to a stiffness drop of 20% with respect to the reference stiffness, measured at the 1000th cycle, while the run-out condition was set to 10^7 cycles. For $R = -1$, five different stress levels were investigated with two tests for each level. This experimental plan gives a replication index, defined according to [46], of 50% that is compliant for research and development testing. The five stress levels investigated were set to 8 MPa, 4.5 MPa, 3.5 MPa, 3 MPa ad 2.5 MPa, giving durations that range from about 2×10^4 to 5×10^6 cycles. The fatigue limit was found with the modified staircase method, as proposed in [47], with 5 tests. To investigate the effect of the mean stress, we carried out six tests at three stress levels for three different stress ratios: $R = 0$, $R = 0.5$ and $R = -\infty$.

Table 2 reports the data of constant amplitude tests. Together with test ID number, stress amplitude σ_a, stress ratio R and reference stiffness K_0, the number of cycle at damage initiation N_i and the number of cycles to failure, computed using different definitions, are listed. The number of cycles at damage initiation was determined according to [28], as the number of cycles at which we observe an increment of 1% of the strain amplitude. The identification procedure is illustrated in Figure 2a, where the evolution of the strain amplitude ε_a (blue dots) is plotted along the number of cycles for Test CA8. The solid line is the 1% offset line, computed with respect to the average of the strain amplitude between cycles 10^3 and 10^4, while the red dot spots the number of cycles at damage initiation. The number of cycles to failure $N_{f,D}$ was defined according to [28], as shown in Figure 2b. Here on the x-axis is

the number of cycles, while on the y-axis is the mean strain, ε_m. The green dots are the experimental points, the solid line is the ratcheting line, defined as the interpolation of ε_m up to the number of cycles at dame initiation, while the dashed line is the interpolation of the last points of the chart [28]. $N_{f,D}$ is defined as the intersections of the two interpolating lines, and it is spotted in the plot by the red circle. Previous literature works [28, 48–51] proved that these two quantities are suitable to identify the points corresponding to damage initiation and damage propagation (i.e. failure). However, for variable amplitude fatigue tests, they cannot be determined, as the stress amplitude and the mean stress are not constant trough the test, thus making impossible to define the 1% offset line and the ratcheting line. To overcome this issue, we defined the number of cycles to failure from the specimen stiffness drop $\Delta K/K_0$, as the cycles at which we observe a given percentage drop. Table 2 reports the number of cycles corresponding to a drop of 2%, 5% and 20%, $N_{f,2\%}$, $N_{f,5\%}$ and $N_{f,20\%}$ respectively. We found that the number of cycles with 2% of stiffness drop, $N_{f,2\%}$, is very similar to the number of cycles at damage initiation, N_i. As can be seen from the plot in Figure 2c, where $N_{f,2\%}$ is plotted versus N_i in double log-scale, the points, with different marks according to the stress ratio, are aligned on a line with unitary slope and passing from the origin (dashed line), and most of them falls into the 20% error bands, highlighted in light blue. Similarly, from the plot

Table 2 – Results of constant amplitude fatigue tests: stress amplitude σ_a, stress ratio R, reference specimen stiffness K_0, number of cycles at damage initiation $N_{f,i}$, number of cycles at damage propagation $N_{f,D}$ number of cycles to failure corresponding to a stiffness drop of 2%, 5% and 20%

ID #	σ_a [MPa]	R	K_0 [N/mm]	N_i	$N_{f,D}$	$N_{f,2\%}$	$N_{f,5\%}$	$N_{f,20\%}$
CA1	8.0	-1	20914.0	15554	29749	17004	27456	29768
CA2	8.0	-1	20780.9	14967	24830	15890	23253	25135
CA3	4.5	-1	21003.0	121518	248101	121459	204341	254040
CA4	4.5	-1	21352.9	142824	251718	161413	223475	263082
CA5	3.5	-1	20913.4	307393	441720	340198	406964	448861
CA6	3.5	-1	21194.9	450240	595979	514915	584285	627280
CA7	3.0	-1	20850.4	819887	1023180	863649	994095	1028098
CA8	3.0	-1	21195.2	1092471	1272339	1129062	1223624	1284325
CA9	2.5	-1	20741.1	4430892	5479111	4968554	5389242	5534026
CA10	2.5	-1	21480.8	3143150	3434647	3249888	3503270	3647203
CA11	2.0	-1	20633.3	6445048	8234185	7378690	7919788	8512332
CA12	2.0	-1	21341.1	*Run-out*: $N_{RO} = 10^7$, $\Delta K/K_0 = -1.55\%$				
CA13	2.0	-1	20747.4	*Run-out*: $N_{RO} = 10^7$, $\Delta K/K_0 = -0.27\%$				
CA14	1.5	-1	20933.8	*Run-out*: $N_{RO} = 10^7$, $\Delta K/K_0 = -0.89\%$				
CA15	4.5	0	20769.7	71852	121230	86943	115555	121291
CA16	4.5	0	20505.7	62405	112479	73019	108181	113064
CA17	3.5	0	20918.2	218776	302921	204381	283464	308972
CA18	3.5	0	21398.7	201270	310101	241082	289550	311037
CA19	2.5	0	21038.5	1369760	1820641	1614890	1761333	1832353
CA20	2.5	0	20521.7	1745995	1957207	1850468	1922174	1963227
CA21	3.5	0.5	20586.5	155814	214898	182967	210648	215242
CA22	3.5	0.5	20642.8	152197	218282	156594	211302	219068
CA23	2.5	0.5	20005.6	679862	891318	819894	880354	897913
CA24	2.5	0.5	20943.2	1019257	1258146	1148783	1229112	1263312
CA25	2.0	0.5	20768.6	3631209	3948306	3781712	3871346	3953669
CA26	2.0	0.5	20959.7	4809632	7220938	6203150	7146118	7224534
CA27	6.0	$-\infty$	21130.4	87090	190049	79461	138390	217453
CA28	6.0	$-\infty$	20698.4	84675	184218	76403	135666	210975
CA29	4.5	$-\infty$	21042.2	378343	704114	238418	521059	846970
CA30	4.5	$-\infty$	20985.1	358552	769157	298770	545251	898414
CA31	3.5	$-\infty$	21053.2	3975428	9098889	3484358	6892678	9688832
CA32	3.5	$-\infty$	21100.7	4117164	*Run-out*	3053253	6724115	*Run-out*

in Figure 2d, where $N_{f,20\%}$ is plotted versus $N_{f,D}$, we can infer that the number of cycles with 20% of stiffness drop is almost equal to the number of cycles at damage propagation. In conclusion, these results show that the point of damage initiation can be well described by $N_{f,2\%}$, while the failure can be characterized by $N_{f,20\%}$. As a consequence, $N_{f,20\%}$ is assumed as the point of fatigue failure and will be referred to as N_f in the following part of the manuscript.

Table 3 reports the results for the modified staircase method [47] for the identification of the fatigue limit at R=-1. The stress level was set initially to 2.5 MPa and subsequently it was increased or deceased by 0.5 MPa, depending whether we observed a failure or a run-out. Besides the five tests that were actually carried out, a fictitious test was added, as indicated in [47], at a stress level of 2 MPa, as the last test ended with a failure at 2.5 MPa. The fatigue limit, $\sigma_{a,lim}$, computed as the average of the tests in the up-down sequence, resulted to be

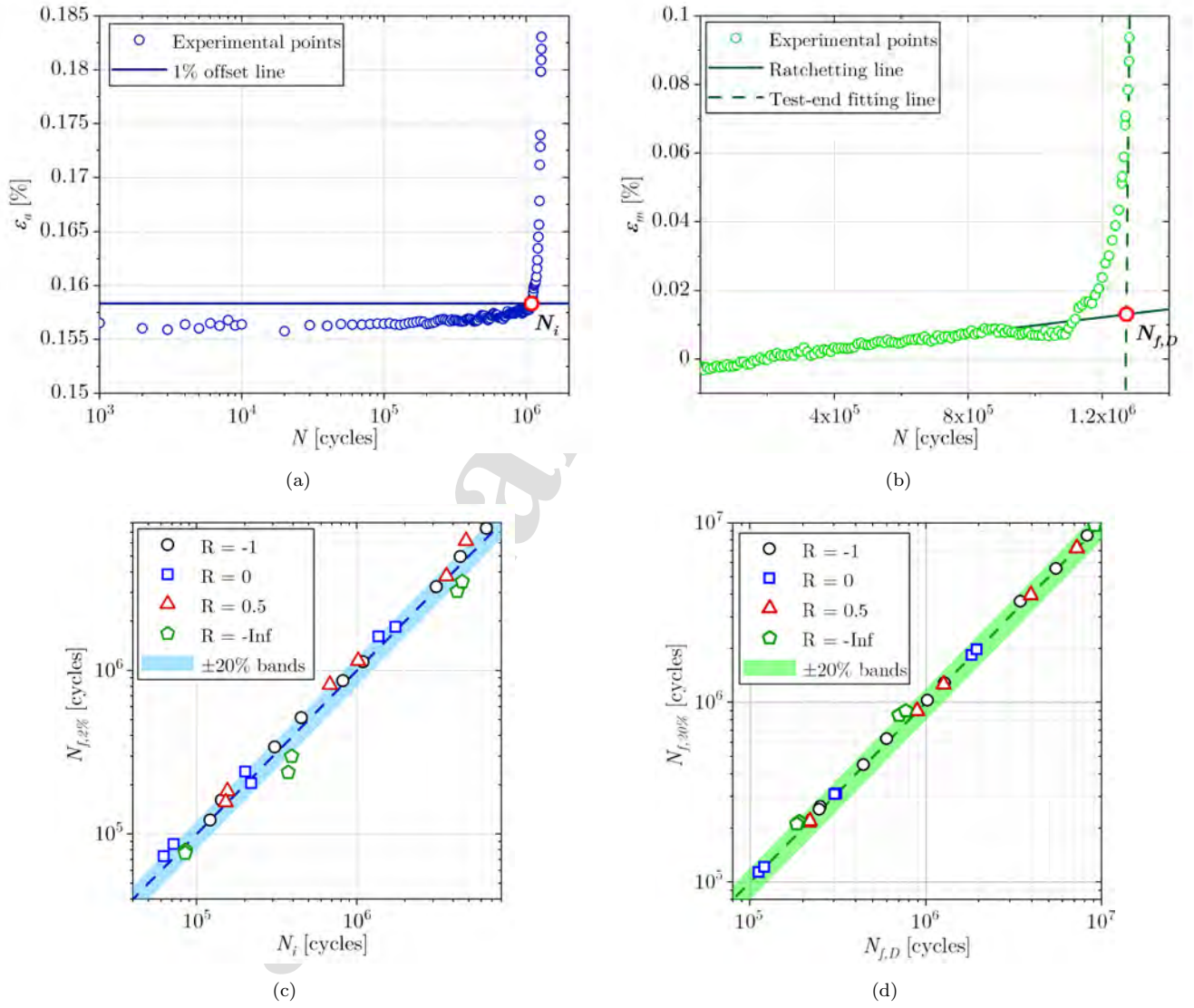

Figure 2 – (a) Identification of number of cycles at damage initiation N_i and (b) number of cycles to failure $N_{f,D}$ [28] for Test CA8, (c) plot of $N_{f,2\%}$ versus N_i, (d) $N_{f,20\%}$ versus $N_{f,D}$

2 MPa. Figure 3 shows the results of the constant amplitude tests on the S-N diagram, for all the stress ratios considered. The plot reports the stress amplitude σ_a versus the number of cycles to failure N_f, in log-log scale. We observe that a positive mean stress has a detrimental effect on the life, as tests conducted at R=0 and R=0.5 lie below those at R=-1. On the contrary, the application of a negative mean stress leads to longer fatigue lives, as can be inferred considering tests at R=$-\infty$.

Table 3 – Results of the modified staircase method [47] for the identification of the fatigue limit at R=-1, where failure (symbol ×), run-outs (symbol ○) and fictitious test (symbol ∗) are reported for the corresponding stress level σ_a

σ_a [MPa]	Modified Staircase									
2.5	×						×			
2			×			○				∗
1.5					○					

× failure, ○ run-out, ∗ fictitious test

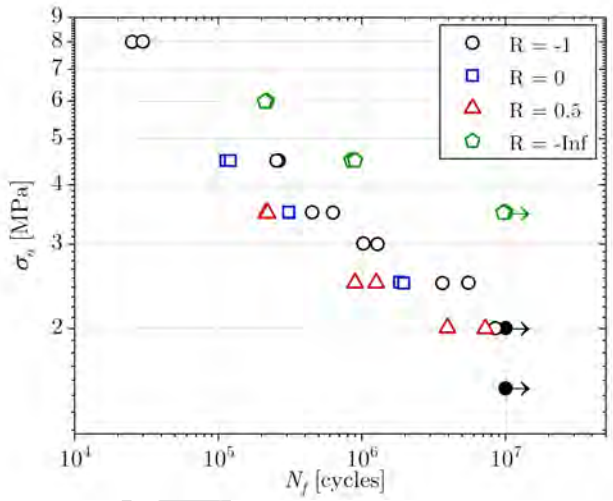

Figure 3 – S-N diagram for tests at constant amplitude with different stress ratios

2.3. Random fatigue tests

Random fatigue tests were carried out in force control with the equipment described for constant amplitude fatigue tests, by applying a suitable stress time-history extracted from random signals. As for constant fatigue tests, test end condition was set to a drop of 20% of the stiffness, with respect to the reference, computed at the thousandth cycle. To generate the stress time-history, we started from a signal sampled for 40 s obtained by the power spectrum density (PSD) of the stress in the most critical point of an industrial heat-exchanger subjected to random vibrations [52]. The reference PSD has a root mean square (RMS) of 1.80 MPa, thus also the reconstructed time signal has the same RMS. Figure 4a shows the PSD of the signal, while Figure 4b shows a signal in time extracted from the PSD. The turning points (i.e. the points where the direction of the load is reversed) were extracted and resampled at a constant frequency of 35 Hz. The signal was then adapted to different RMSs with a

suitable amplification factor. Cycles with an amplitude lower than half of the fatigue limit were removed to speed up the tests, as no damage associated to them is expected. The resampling and filtering procedure on the time history was performed with a dedicated routine in Matlab that, given a random signal, extracts the turning points and compute the amplitude according to the Rainflow method [53]. Each time signal used for experimental tests contains approximately 28000 turning points or 14000 cycles and it is repeated up to failure (i.e. the applied stress history is composed by the loop repetition of a random signal sampled at constant frequency).

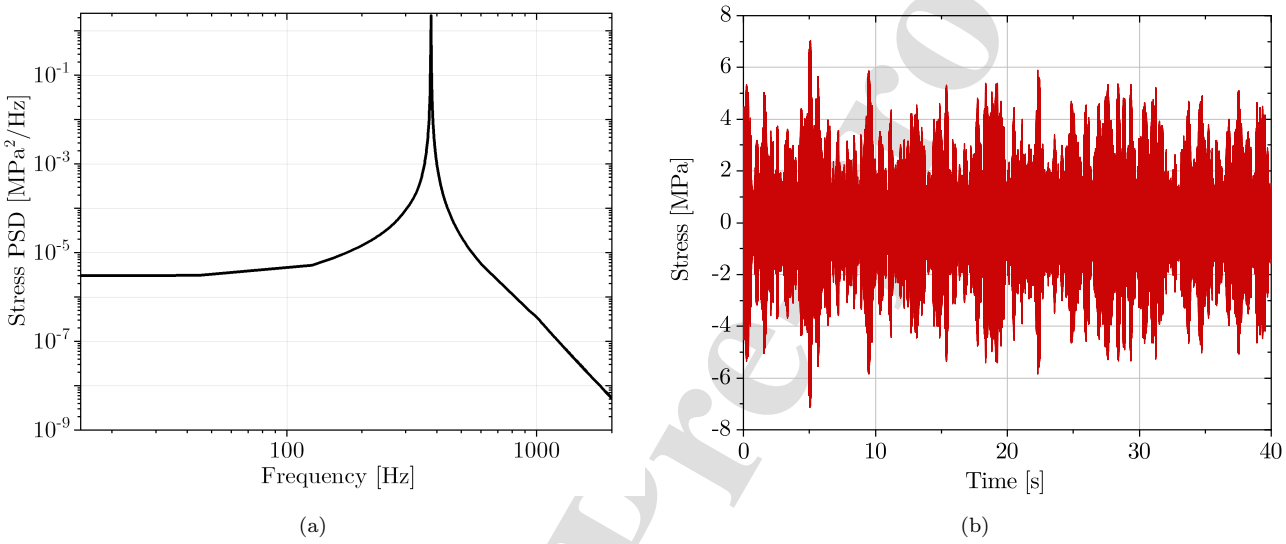

Figure 4 – (a) PSD used to reconstructed random signals and (b) random signal sampled for 40 s with RMS=1.80 MPa

A total of 9 specimens were tested under random fatigue loading conditions. 6 samples were tested with a signal with time average equal to zero, as the one shown in Figure 4, with 4 different RMS levels. Other 3 samples were tested with a signal with positive time-average $\bar{\sigma}$, obtained by adding an offset equal to the value of the RMS of the original signal. These tests were carried out to evaluate the effect of a mean stress upon fatigue life under variable amplitude conditions. Table 4 reports, for each test, the RMS of the original applied spectrum, the crest factor CF, defined as the maximum stress in time over the RMS, the stress time-average, the reference specimen stiffness and the number of cycles to failure corresponding to a stiffness drop of 2%, 5% and 20%.

Table 4 – Results of random fatigue tests: RMS of the signal, signal crest factor (CF), time-average of the signal, reference specimen stiffness and number of cycles to failure corresponding to a stiffness drop of 2%, 5% and 20%

	RMS [MPa]	CF	$\bar{\sigma}$ [MPa]	K_0 [N/mm]	$N_{f,2\%}$	$N_{f,5\%}$	$N_{f,20\%}$
Test 1	1.80	4.23	0	19671.2	704842	1240104	1608310
Test 2	2.08	3.82	0	20748.6	341882	648152	849765
Test 3	3.12	3.81	0	20658.8	99241	178434	207058
Test 4	2.08	4.27	0	21143.7	263663	591011	730739
Test 5	1.25	3.79	0	20780.5	2331110	3174203	3858900
Test 6	1.25	3.36	0	20437.1	2555504	3400415	4013305
Test 7	2.08	4.57	2.08	20740.9	247759	465389	498700
Test 8	1.25	4.14	1.25	21471.7	1569883	3045335	3458700
Test 9	3.12	4.09	3.12	20609.8	72235	112815	115700

In figure 5, the RMS of the random signal used for the tests is plotted against the number of cycles to failure, in a double logarithmic scale. The points for tests with zero time-average are plotted in red, while data for tests with positive time-average are plotted in blue. The data are well aligned in the chart, showing that the relation between the logarithms of RMS and N_f is linear. Coherently with constant amplitude fatigue tests, those with time-average higher than zero exhibit a shorter life.

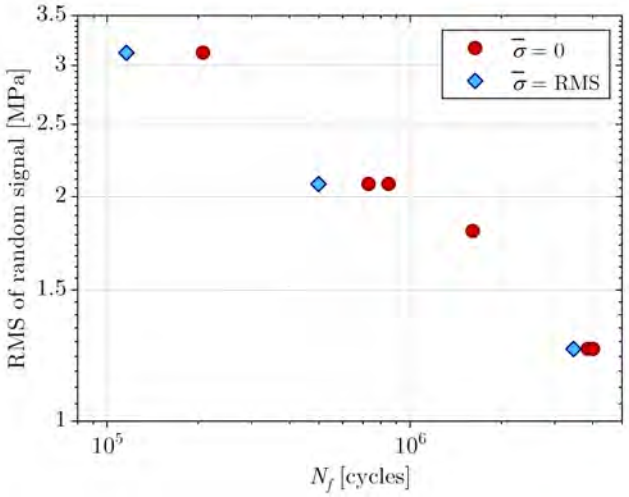

Figure 5 – Endurance curve for random fatigue tests: RMS of the random signal versus number of cycles to failure

2.4. Analysis of failure mechanisms and fracture surfaces

After fatigue testing, some samples were statically broken to characterize the failure mechanisms, and to study how they are affected by the stress ratio. Tests performed at variable amplitude and constant amplitude at R=-1 are characterized by similar failure mechanisms, with cracks propagating perpendicularly to the load direction. Figure 6 shows a three dimensional picture of the fracture surfaces of six different tests. For constant amplitude tests at R=-1 and higher stress levels (top-left panel), we observe the coexistence of two failure mechanisms. The

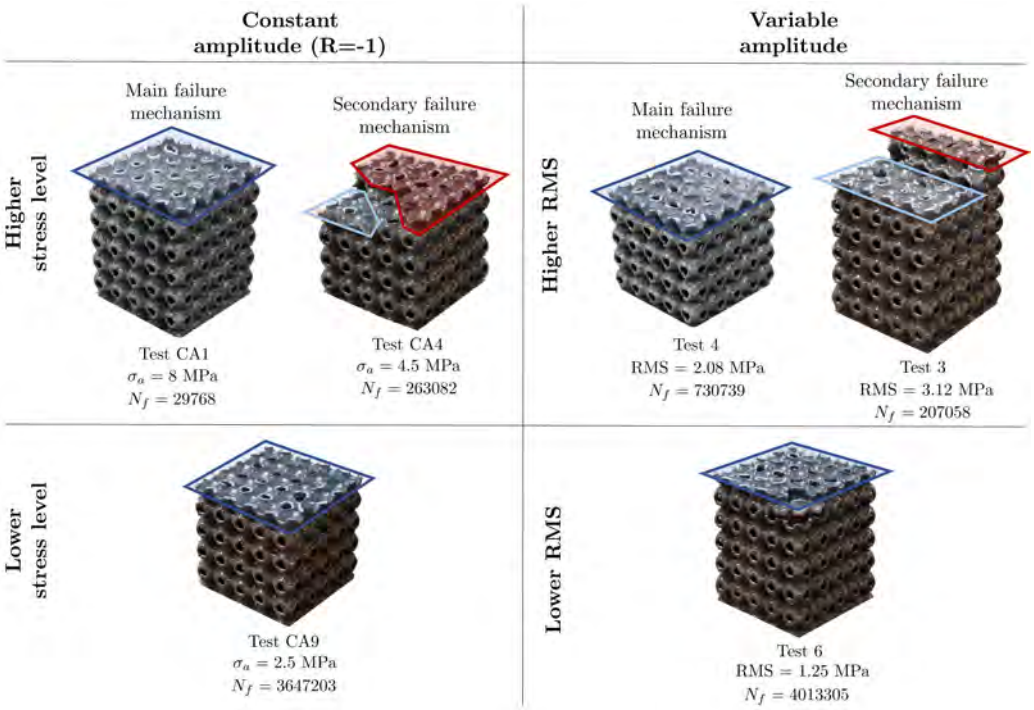

Figure 6 – Failure mechanisms analyses for constant amplitude at R=-1 and variable amplitude fatigue tests

main one is characterized by a single fracture plane (highlighted in blue), while the secondary one is characterized by a fracture on two different planes (highlighted in light-blue and red). The secondary failure mechanisms was observed with a lower frequency, approximately one sample over six, and it is caused by the activation of multiple initiation points, that leads to cracks propagating on different planes. For tests at constant amplitude and lower stress levels (bottom-left panel), we observe only one failure mechanism, with single-plane fracture, as the lower stresses activate a lower number of initiation points. Similar considerations can be drawn for variable amplitude tests (top and bottom right panel), characterized by the same failure mechanisms, depending on the RMS level.

For a better understanding of the exact position of the cracks in the cell, some fracture surface were analysed with a Scanning Electron Microscope (SEM). Figure 7 shows the fracture surfaces of two specimens tested at constant amplitude at R=-1. The sample in Figure 7a (Test CA4, see Table 2) was tested at a stress level of 4.5 MPa, with a duration of 2.6×10^5 cycles, while the sample in Figure 7b (Test CA9) was tested at a stress level of 2.5 MPa, with a duration of 5.5×10^6 cycles. Test CA4 (Figure 7a) is characterized by the two-planes failure mechanism as reported in the section view in top-left. The orange circles indicate the cells totally failed by fatigue, as the one in detail A. In particular, we can distinguish two cracks propagated up to the total failure of the cell, starting from two planes with a slight offset. The yellow circles mark the cells whose failure is characterized both by fatigue and by static failure, as the one in detail B, where most of the surface is broken statically and only a small and not-propagated crack is present in the bottom part. Looking at the cell wall in the upper left part of the picture, the manufacturing layers, parallel to the picture plane, can be distinguished. In the magnified picture (bottom-right) it is possible to spot two nucleation points of the crack, in correspondence of surface defects, while the remarkable presence of internal defects (mainly pores) does not lead to crack nucleation, in agreement with

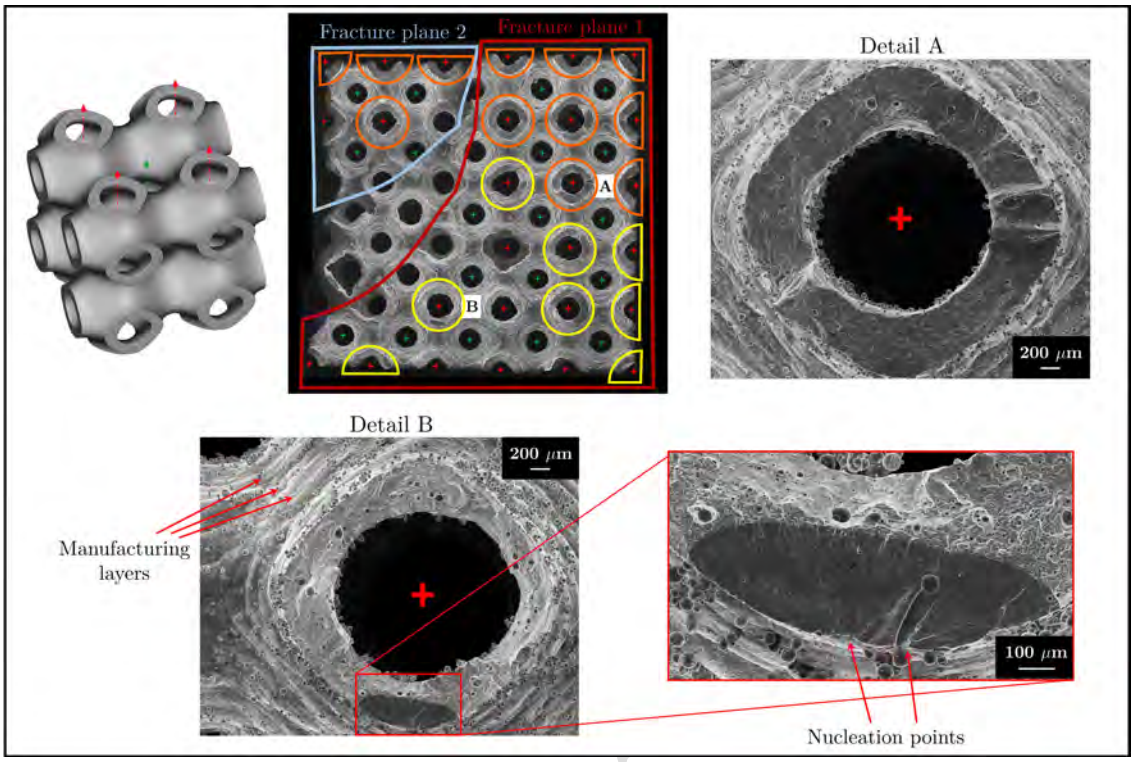

(a)

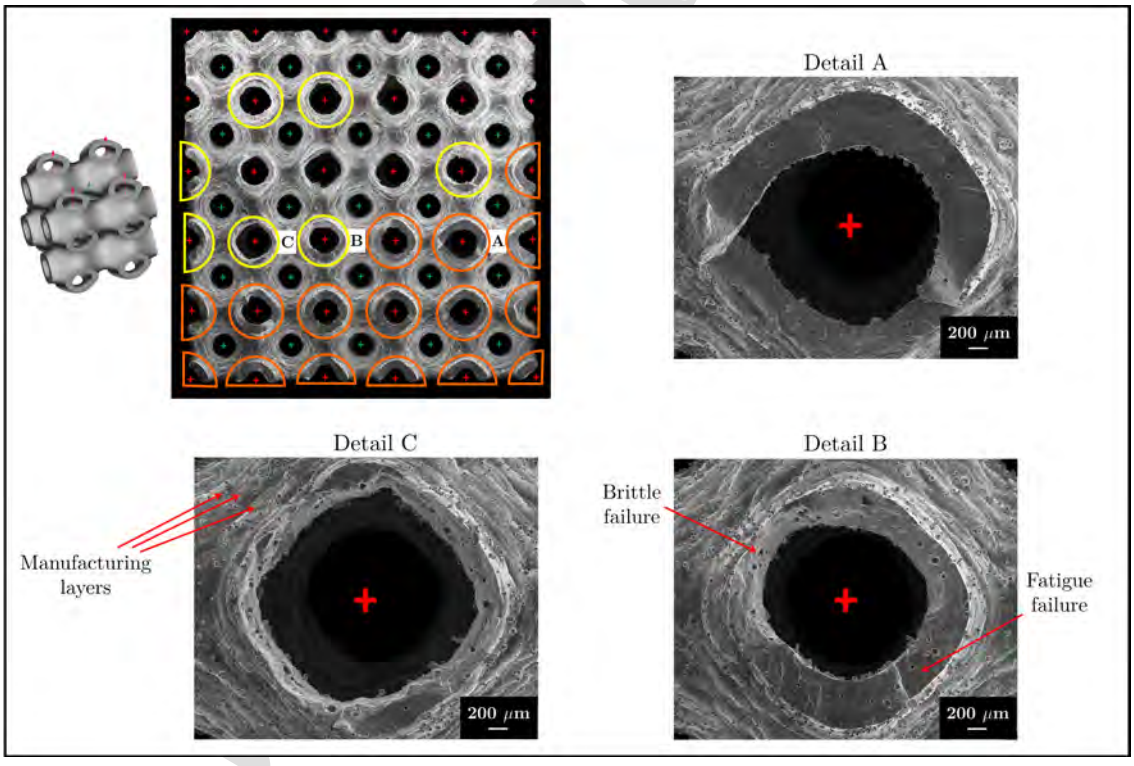

(b)

Figure 7 – Fracture surfaces of samples tested under variable amplitude at R=-1: (a) Test CA4 (σ_a = 4.5 MPa) and (b) Test CA9 (σ_a = 2.5 MPa)

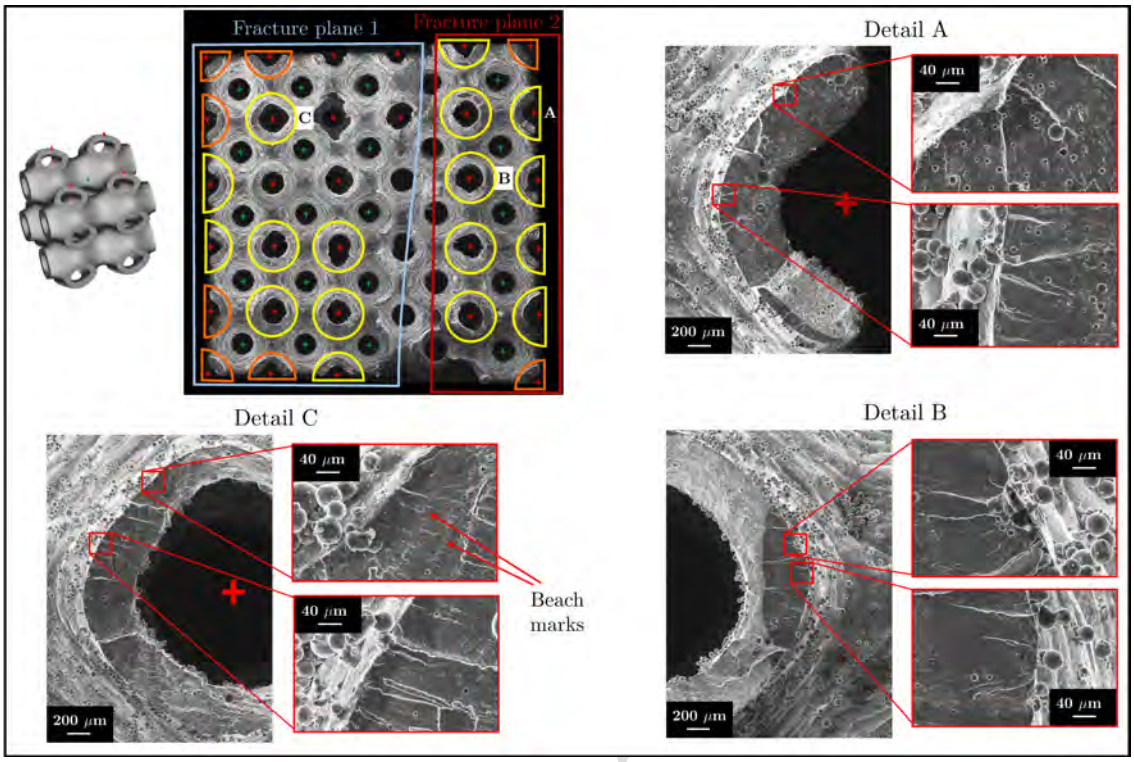

(a)

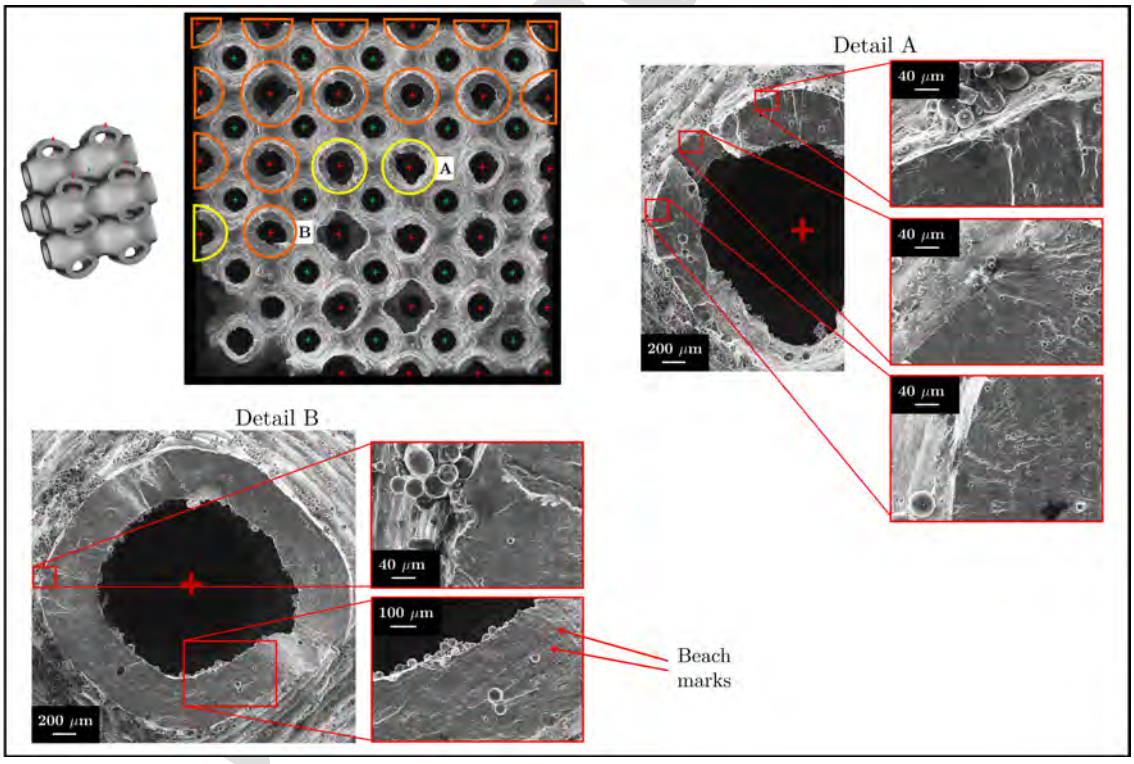

(b)

Figure 8 – Fracture surfaces of samples tested under variable amplitude: (a) Test 3 (RMS=3.12 MPa) and (b) Test 6 (RMS=1.25 MPa)

previous observations [28]. Test CA9 (Figure 7b) is characterized by a single plane of fracture, with the broken cells concentrated on the bottom part of the section, differently from what observed for test CA4, where the broken cells are more distributed on the entire surface. This difference can be attributed to the different stress level, as lower stress amplitudes activate a lower number of nucleation points, thus favouring the localization of the damage in the section. Detail A shows a cell totally broken by fatigue; also in this case two cracks can be seen, propagated on two planes with a slight offset. Detail B shows a cell with a crack that propagated for almost half of the fracture surface (bottom part), from which it is possible to clearly spot the differences between brittle failure and fatigue failure. Finally, detail C shows a cell mainly characterized by brittle failure, with two small and not-propagated cracks, nucleated from the outer surface of the cell wall.

The analyses of the fracture surfaces of samples tested under variable amplitude fatigue conditions reveal a failure mechanism very similar to the one observed for constant amplitude tests. Figure 8 shows the fracture surfaces of specimens tested under random fatigue, Test 3 (Figure 8a) and Test 6 (Figure 8b). Test 3 was performed at the highest level of RMS, i.e. 3.12 MPa, while Test 6 at the lowest level of RMS, i.e. 1.25 MPa, both of them with zero time-average (see Table 4). The fracture surface of test 3 shows two planes of fracture, with cracks spread along the entire section, and a prevalence of cracks that do not lead to the failure of the entire cell, as those in detail A, B and C. On the contrary, the fracture surface of Test 6, i.e. the test at lower RMS, shows a more localized presence of cracks in the upper part of the section, with a prevalence of cracks that propagated up to the failure of the entire cell, as the one in detail B. As observed for constant amplitude tests, all the cracks nucleated from surface defects, in correspondence of small scratched, imperfections or powder particles stuck on the surface (spatter), while no cracks are originated by internal defects. Finally, by looking at detail C in Figure 8a and detail B in Figure 8b, beach marks of crack propagation can be observed, as a consequence of the peak stresses, which lead to a not-constant crack propagation rate.

The analyses carried out on specimens tested at R=0 and R=0.5 show that the failure mechanism is practically not affected by positive mean stress. The samples show one or two fracture planes perpendicular to the load directions. On the contrary, the failure mechanism of samples tested at R=-∞ differs significantly. As shown by the three dimensional picture in Figure 9, pertinent to test CA29, the fracture surface is jagged and not planar. The SEM top view of the section (top-right images) shows the presence of one single crack (detail A) in the $x-y$ plane, while several cracks can be seen in the other two planes perpendicular to the one of the image. The SEM side view ($y-z$ plane) in the bottom part of the figure confirm that, for this load ratio, cracks propagate also in the planes parallel to the load direction, as the one highlighted in detail B, consequently to the different local stress distribution in the cell.

3. Analysis of constant amplitude tests results

3.1. Numerical analyses

To corroborate the fracture surfaces analyses presented in the previous section and to better elucidate the fatigue failure mechanisms of the investigated TPMS structure, numerical analyses were carried out. The goal of such analyses is to identify the location inside the cell of the most critical points for fatigue failure, from which

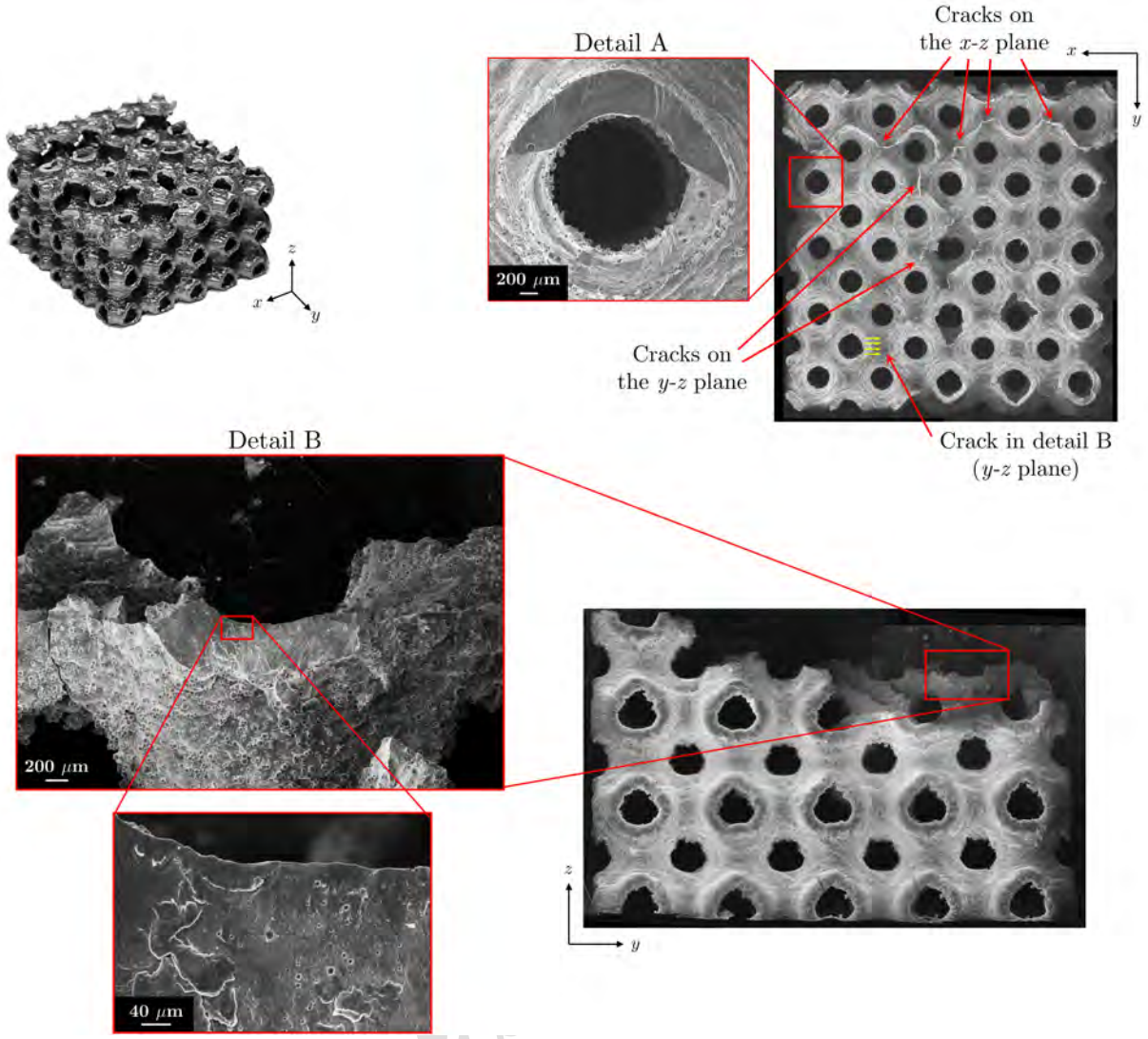

Figure 9 – Fracture surface analysis of test CA29, tested at R=-∞: 3-dimensional picture, top view and lateral view

cracks might originate. To this aim, we adopted the numerical framework developed in [28], which consists in a local stress approach based on the critical distance theory [54] which compute an equivalent amplitude stress from the results of finite element analyses. The framework is implemented in an in-house built Matlab[1] routine, linked with the commercial FE solver Abaqus[2]. CT scan were performed on a portion of one sample, with a NSI X-25 system and a resolution of 19.2 μm/voxel, to reconstruct the as-built geometry. One cell was analysed, with periodic boundary conditions. In the analyses, we used the properties of the base material reported in Table 1, the fatigue limit at R=-1 was estimated as 75 MPa [55], while the critical distance value was assumed equal to 100μm. We emphasize that, despite simulating one single cell does not provide any information about the statistical variability in the specimen of local stresses, target of these analyses is to evaluate the distribution of the local stresses inside

[1]Matlab, MathWorks, United States
[2]Abaqus, Dassault Systèmes Simulia Corp, United States

the reference volume element and not to provide a numerical estimation of the fatigue strength to be compared with experimental results.

Figure 10 shows the plot of the local equivalent stress amplitude $\sigma^{[s]}_{a,eq}$, normalized with respect to the base material fatigue limit $\sigma^{[s]}_{a,lim}$. The superscript $[s]$ stands for 'solid' and indicates that the quantity refers the solid material and not to a homogeneous quantity. $\sigma^{[s]}_{a,eq}$ is evaluated as the Sines equivalent stress, as proposed in [28]. The analyses were conducted for 3 different stress ratios, R=-1, R=0 and R=-∞. Looking at the figure, where z represents the loading direction, it is clear that the location of the most critical points is similar for R=-1 and R=0, while it is different for R=-∞. In the first two cases, the critical regions are slightly below the upper end of the cell and slightly above the lower end, and are almost aligned on the $x-y$ plane. Instead, for the last case, where the cell is subjected to compressive load for the entire load cycle, the critical points are in the region subjected to tension of the lateral cavities. It is reasonable to expect that these points are the nucleation points of the cracks in the planes parallel to the loading direction observed from the fractography of the samples tested at this stress ratio (see Figure 9). In conclusions, the numerical analyses show that the position of critical points for fatigue failure change accordingly to the stress ratio, thereby corroborating the experimental observation of different failure mechanisms.

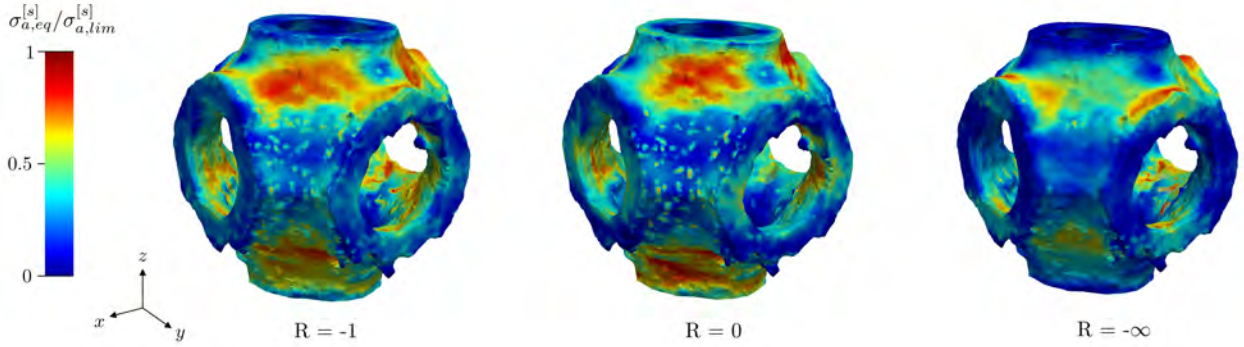

Figure 10 – Results of the numerical analyses to individuate the most critical points for fatigue failure [28], performed on a cell with as-built geometry: normalized local equivalent stress amplitude for three different stress ratios

3.2. S-N curve estimation

The fitting of the S-N curve was performed on the results of experimental tests at R = -1, considering only failures. The number of cycles to failure of each test was set as the cycle at which we observed a drop of the stiffness of 20%, as discussed in section 2.2. As proposed by ISO standard 12107 [47], the S-N diagram data can be fitted with a linear regression in the double log plane. Defined N_f the number of cycles to failure and σ_a the alternate stress, the relations between the two quantities is:

$$\log_{10}(N_f) = b_0 + b_1 \log_{10}(\sigma_a) \tag{1}$$

The standard deviation of the dependent variable, $\sigma_{\log N}$, is computed as:

$$\sigma_{\log N} = \sqrt{\frac{\sum_{i=1}^{n} \left(Y_i - \hat{Y}_i\right)^2}{n-p}} \tag{2}$$

where n is the number of samples used for the fitting, $p = 2$ is the number of estimated parameters, Y_i is the base 10 logarithm of the number of cycles to failure of the i-th experimental observation (i.e. $Y_i = \log_{10}(N_{f,i})$) and $\hat{Y}_i$ is the base 10 logarithm of the model estimate for the i-th observation according to Equation 1.

Figure 11 shows the results for constant amplitude fatigue tests at R=-1 and the fitting of the S-N curve. The parameters of the fitting and the curve dispersion $\sigma_{\log N}$, computed according to Equation 2, are listed in Table 5. To account for possible damage in the infinite-life region ($\sigma_a < \sigma_{a,lim}$), the Haibach rule [56, 57] was used.

Table 5 – Parameters of the fitting and curve dispersion for linear regression, according to Equations 1

	b_0	b_1	$\sigma_{\log N}$
S-N curve parameters	8.14	-4.23	0.13

3.3. Equivalent stress amplitude definition

The definition of the equivalent stress amplitude is functional to correctly consider the effect of the mean stress in the damage for the analysis of random test results. In fact, even if the stress applied has zero time-average, some cycles might have a mean component, thus requiring a correction of the amplitude. For our data, we found that a combination of the classical corrections proposed by Goodman and Soderberg well describes the effect of mean stress. The equivalent stress amplitude, $\sigma_{a,eq}$, is computed according to the Goodman equation if the mean stress is positive while, if the mean stress is negative, the Soderberg equation is adopted. This choice is motivated by the different failure mechanisms observed, depending on the sign of the mean stress. Defined σ_a and σ_m the alternate and the mean component of the cycle, and σ_y and UTS the yielding and ultimate effective strength (see Table 1),

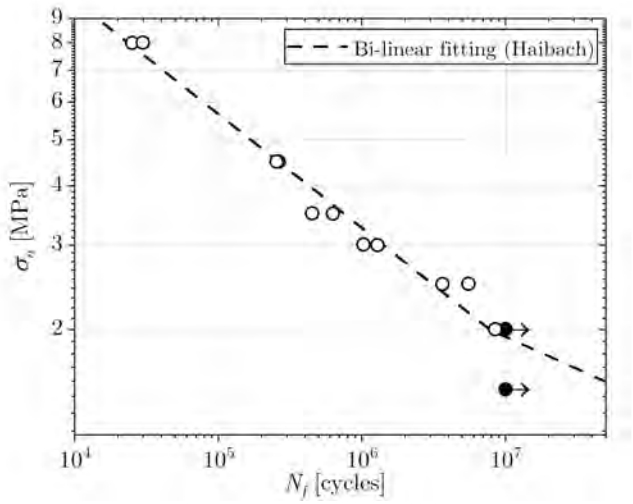

Figure 11 – Constant amplitude fatigue curve (R=-1) of AlSi10Mg Schwarz primitive TPMS (experimental points and bi-linear curve with Haibach rule)

it follows the definition of $\sigma_{a,eq}$:

$$\sigma_{a,eq} = \begin{cases} \dfrac{\sigma_a}{1 - \dfrac{\sigma_m}{UTS}} & \text{if } \sigma_m \geq 0 \\ \dfrac{\sigma_a}{1 - \dfrac{\sigma_m}{\sigma_y}} & \text{if } \sigma_m < 0 \end{cases} \tag{3}$$

In Figure 12, the equivalent stress amplitude (Equation 3) is plotted against the number of cycles to failure. Together with the results the regression line (dashed black line) computed from tests at R=-1 and the 95% scatter bands (dotted black lines) are reported. For R=0 (blue squares), the points are aligned on the regression line, showing that the model for the equivalent stress amplitude we adopted is appropriate for this stress ratio. For tests conducted at R=0.5 (red triangles) and R=$-\infty$ (green pentagons), the points for the two highest stress levels are inside the scatter bands of the S-N curve and, overall, they are aligned with the points for R=-1. Instead, for the lowest stress level, we observe that one test at R=0.5 and the two tests at R=$-\infty$ are outside the confidence bands and close to the fatigue limit. The presence of these points outside the scatter bands might indicate that the model proposed in Equation 3 is not fully able to describe the effect of the mean stress on the life for some specific cases (i.e. durations higher than 10^6 cycles). However, as most of the points are inside the scatter bands and given the need of a simple model to handy analyse the random fatigue tests results, we considered the accuracy of our model as acceptable.

4. Analysis of random tests results

As done for constant amplitude fatigue tests, the number of cycles to failure, N_f, was computed as the cycle at which we observe a 20% of stiffness drop, with respect to the reference (stiffness at cycle number 1000). For each test, the load that was applied to the sample was recorded to reconstruct the effective stress history up to failure. The stress history was then analysed with the Rainflow method [53], by means of the dedicated function

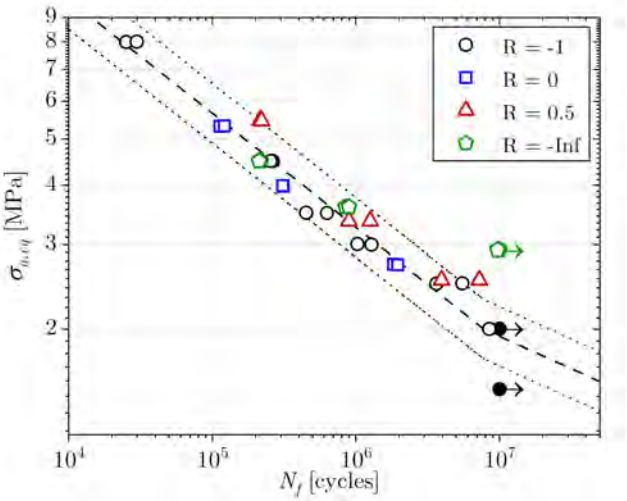

Figure 12 – Equivalent stress amplitude (defined according to Equation 3) versus number of cycles to failue, for experiments carried out at different stress ratios

implemented in Matlab. In this way the time history was decomposed in a series of cycles with a given amplitude and mean component, and, by means of Equation 3, the equivalent amplitude of the given i-th cycle, said ${\sigma_{a,eq}}^{[i]}$, was obtained. Finally, the damage variable D, associated to the test, was computed according to the Miner's rule [44]:

$$D = \sum_{i=1}^{N_f} \frac{1}{\hat{N}_f^{[i]}} \tag{4}$$

where $\hat{N}_f^{[i]}$ is function of the equivalent stress amplitude of the i-th cycle ${\sigma_{a,eq}}^{[i]}$ and is computed according to Equation 1. If the damage evolution under variable loading conditions is well described by the Miner's rule, the damage variable D should assume values close to 1, and the deviation of its base 10 logarithm should correspond to the deviation of the S-N curve (i.e. $\sigma_{\log D} \approx \sigma_{\log N}$) [58–60]. The procedure to evaluate the damage is schematized in Figure 13, where the histogram of the Rainflow counting output is shown, as well as the equivalent stress amplitude histogram together with the S-N curve.

Considering all the tests, the damage variable D is distributed in the range $[0.68, 1.36]$, with values that oscillate around 1. Figure 14a shows the log-normal probability plot for the variable D. The distribution fits well the experimental data: all the points are aligned according to the regression line (solid line) and lie inside the 95% confidence bands (dashed lines). The mean value of the base 10 logarithm of D is 0.0154 while the standard deviation $\sigma_{\log D}$ is 0.115. In agreement with the theory, the standard deviation of the logarithm of the damage is comparable to the standard deviation of the S-N curve ($\sigma_{\log N} = 0.13$, see Table 2) and the modal value of D is approximately 1 (1.036). In Figure 14b, the damage variable is plotted against the RMS of the random signal, showing that all the data are inside the 95% scatter bands of the distribution (dashed black lines, computed according to the fitting in Figure 14a), regardless from the RMS and the time-average. Although the statistical scatter of the damage is coherent with the scatter observed for constant amplitude fatigue life, we observe that tests performed at the lowest

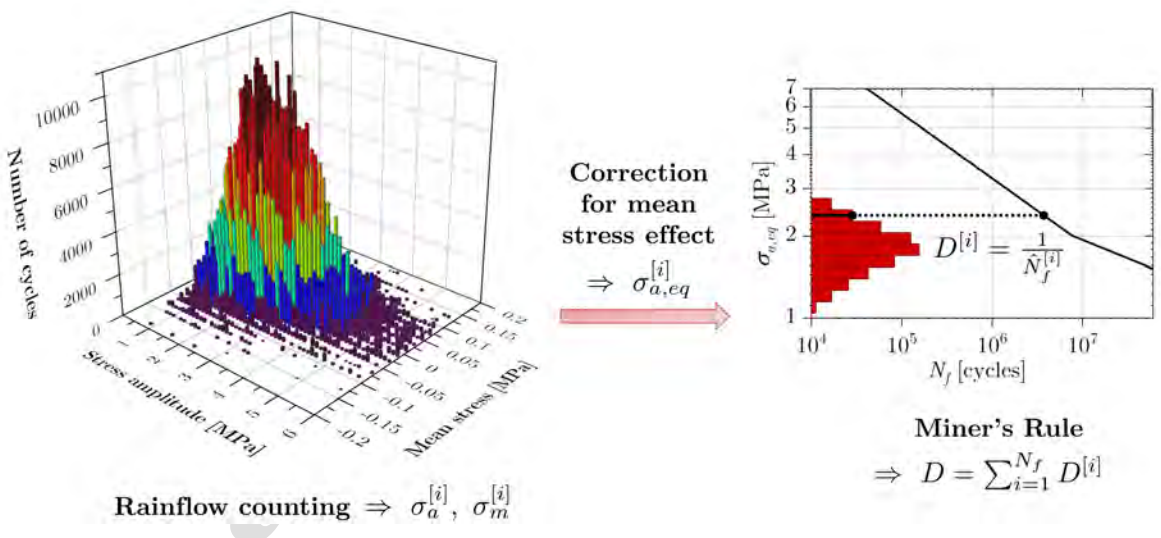

Figure 13 – Computation of the damage associated to the stress history shown in Figure 4: results of the Rainflow counting (histogram for each combination of stress amplitude and mean component), comparison of the equivalent stress amplitude histogram with the S-N curve, after the correction to account for mean stress effect through Equation 3.

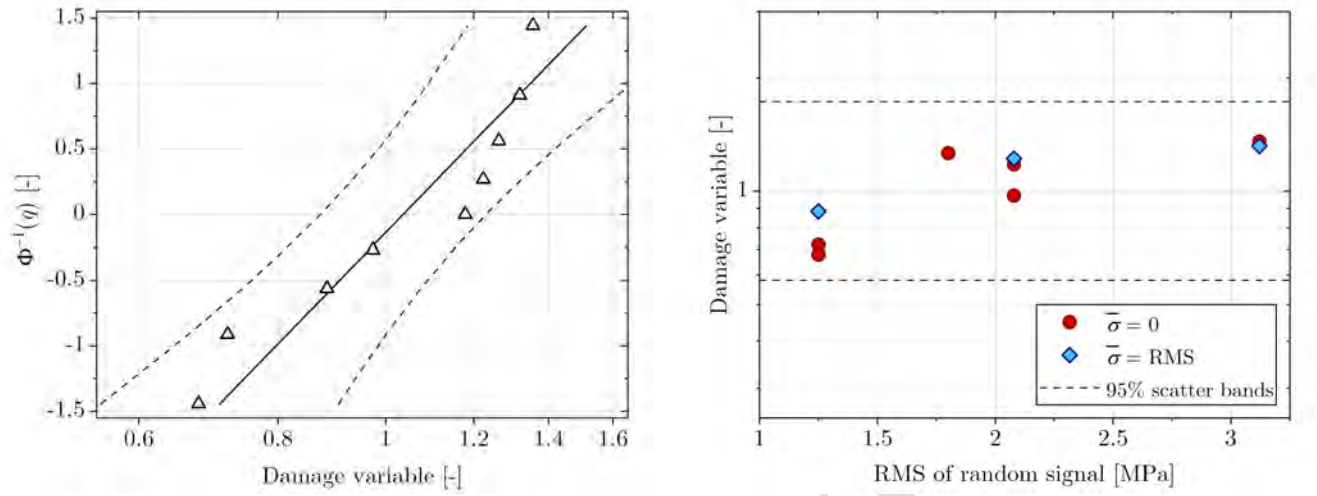

Figure 14 – (a) Log-normal probability plot for the damage variable, (b) damage variable versus RMS of random signal

RMS level (1.25 MPa) show damages lower than 1 (approximately 0.7, see Table 4), despite being inside the scatter bands. Results are discussed in the next session, focusing in particular on this aspect.

5. Discussion of results

The results reported in Section 4 show that random fatigue strength for an aluminium Schwartz lattice could be well described by combining the use of the Miner's rule (Equation 4), the S-N curve at R=-1 and the model proposed in Equation 3 to account for the mean stress effect on the life. The approach proposed to describe damage is similar to the standard methods used for solid materials (see for example [44, 56, 57]), hence simple to be applied and based on solid theoretical fundaments. However, despite the experimental scatter for random fatigue tests parallels the scatter of constant fatigue tests, in this section we discuss the possible motivations underpinning the relatively low damage values observed for tests performed at an RMS level of 1.25 MPa.

Figure 15 shows the evolution of the stiffness drop during the life for Test 3 (RMS=3.12 MPa, Figure 15a) and Test 6 (RMS=1.25 MPa, Figure 15b). On the x-axis is the life normalized by the number of cycles to failure N_f, while on the y-axis is the stiffness drop normalized to the reference stiffness, in percentage. The curves for random tests (red curves) are compared with the results of tests CA4 and CA9 performed at constant amplitude (blue curves) for R=-1 and similar fatigue life (see the legend in the plot). Constant and variable amplitude tests with lower duration (2×10^5 cycles, Figure 15a) show a similar evolution of the stiffness drop during the life, with a progressive decreasing phase up to approximately 0.8 of N_f, with a total stiffness loss of 5%, followed by a phase where the stiffness drop decreases up to specimen failure. These results suggest that both tests are characterized by a progressive damage. On the contrary, constant and variable amplitude tests with higher duration (4×10^6 cycles, Figure 15b) show remarkable differences in the stiffness drop evolution. Random Test 6 (red curve) shows an evolution similar to the one of Test 3 described previously, thus highlighting the presence of progressive damage throughout the entire life. Differently, for constant amplitude test, the specimen stiffness remains unchanged up

to almost 90% of N_f, then a sudden drop can be observed. A similar behaviour was observed also for the other constant amplitude tests performed at low stresses, suggesting that in these cases most of the life is spent in the damage initiation phase.

Similar conclusions can be inferred by observing the portions of life corresponding to a stiffness drop of 2%, 5% and 20%, in the bar plots in Figure 16. Data for all constant amplitude fatigue tests at different stress ratios are shown in Figure 16a while data for all random fatigue tests are shown in Figure 16b. Here on the x-axis is the number of cycles to failure N_f while on the y-axis is the portion of life normalized with respect to N_f. For constant amplitude tests at R=-1 (Figure 16a, top-left), the portion of life corresponding to a stiffness drop lower than 2% (i.e. damage initiation, see Section 3) increases with the number of cycles to failure. Tests with lower durations reach a stiffness drop of 2% at about 60% of the life while tests with higher durations take about 90% of the life. Furthermore, portion of life corresponding to a stiffness drop higher than 5% shows a slightly decreasing trend with the number of cycles to failure. On the contrary, no remarkable differences can be observed among the different random tests (Figure 16b). In this case, all the tests reach a 2% drop of the stiffness at approximately 60% of the life and the portion of life spent for stiffness drop higher than 5% does not show any trend with the number of cycles to failure.

The different evolution of the stiffness drop for random tests can be attributed to the presence of few cycles at high stress levels that modify the damage evolution. Observing the random signal in Figure 4, that has an RMS of 1.80 MPa, we can spot several cycles with amplitude higher than 2 times the value of the RMS (i.e. 4 MPa), with one peak of stress higher than 6 MPa (i.e. about 3.5 times the RMS). Thus, also for tests performed with an RMS of 1.25 MPa we do expect the presence of some cycles with amplitude higher than 3.5 MPa, that might lower the damage initiation phase. Despite the peaks load might not influence particularly the region of shorter lives, characterized by a remarkable portion of life spent in damage propagation and for which we observe damage

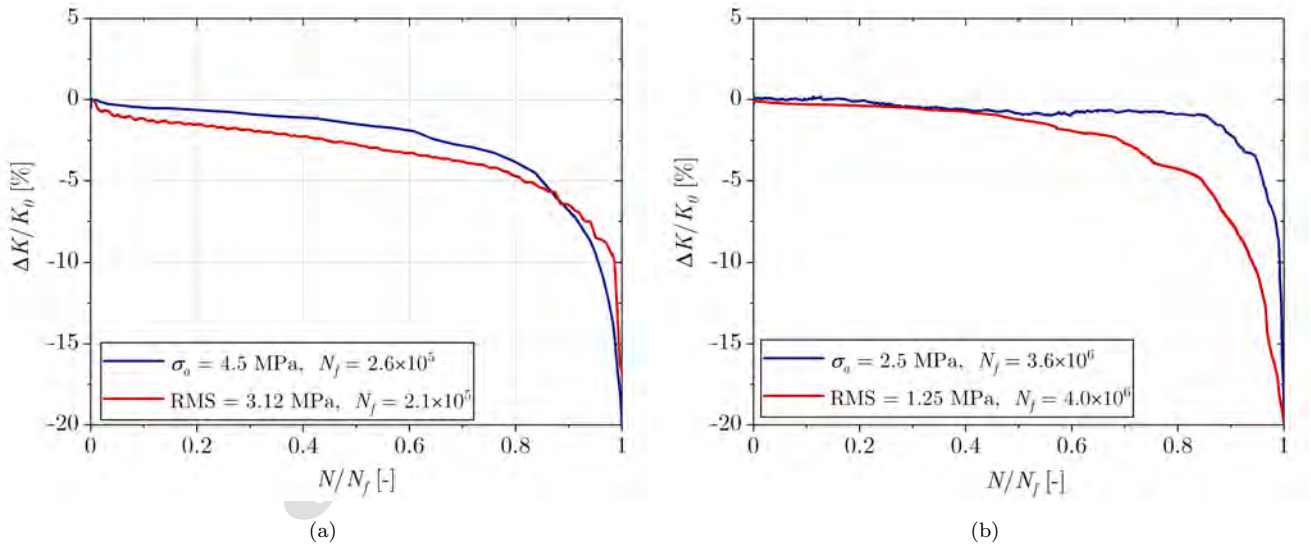

(a) (b)

Figure 15 – Stiffness drop observed during the experiments for (a) Test 3 and (b) Test 6, compared to what observed for tests CA4 and CA9 at constant amplitude and R=-1 with similar duration

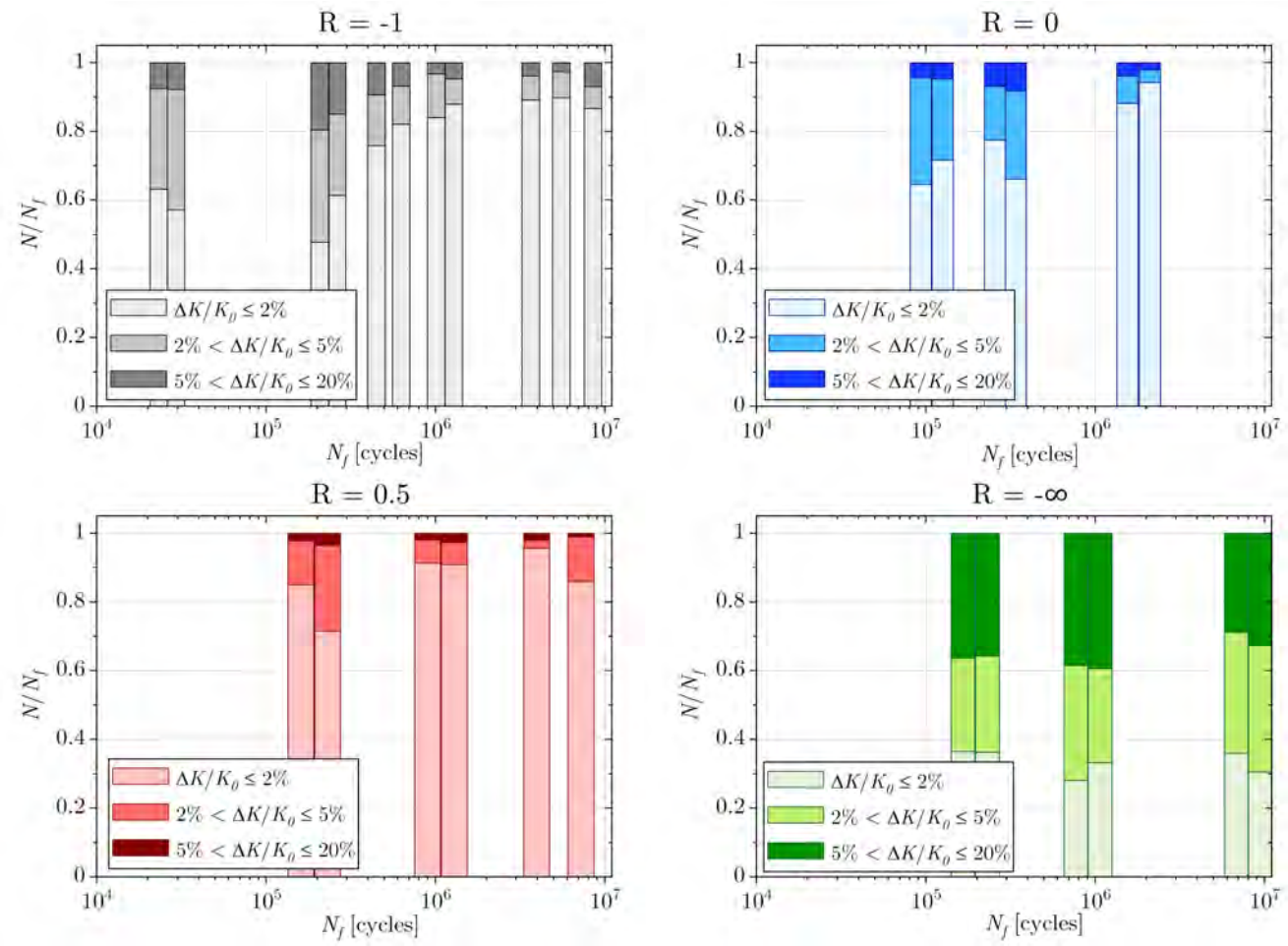

(a)

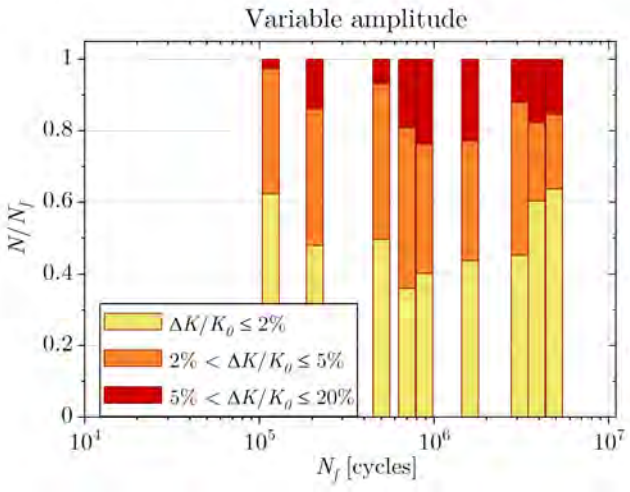

(b)

Figure 16 – Life for different stiffness drop values (0-2%, 2-5% and 5-20%): portion of life (with respect to $N_{f,5\%}$) for (a) constant amplitude test and (b) random fatigue tests

indexes close to the unity, the effect can be dramatically higher in the longer lives region, where almost 95% of the life is spent in damage initiation and for which we observe damage indexes lower than one.

Regarding constant amplitude tests with non-zero mean stress, tests performed at R=0 and R=0.5 shows a behaviour comparable to the one observed for R=-1. On the contrary, tests at R=-∞ shows a different damage propagation: regardless from the duration of the tests, the portion of life needed to initiate damage is almost 40% of the total life, thus suggesting a shorter nucleation phase followed by a long phase of damage propagation. This remark is in agreement with the failure mechanisms analyses, who revealed strong differences between tests with positive mean stress and those with negative mean stress.

6. Conclusions

This paper have addressed constant and variable amplitude fatigue strength of a TPMS Schwarz primitive lattice structure made with AlSi10Mg aluminium alloy. Constant amplitude fatigue life at stress ratio R=-1 was experimentally characterized and the effect of the mean stress on the life was studied by performing tests at stress ratios different from -1. Random fatigue tests were performed with stress histories having different RMS values. Some tests were performed by adding a mean component to the signal equal to the RMS, to study the effect of the mean stress on variable amplitude fatigue. An approach to evaluate the damage evolution under variable loading has been proposed and validated by analysing the experimental results. The remarkable outcomes of this work can be outlined as follows:

- Positive mean stresses have a detrimental effect on constant amplitude fatigue life. This effect can be modelled with a combination of the classical Soderberg and Goodman model. Using the Goodman correction for positive mean stresses and the Soderberg correction for negative mean stresses allows to collapse all the experimental data on the S-N curve fitted for R=-1, regardless from the stress ratio.

- The duration of random fatigue tests shows a linear dependence on the RMS of the signal used for the tests in a double-log chart. As for constant amplitude fatigue tests, introducing a positive mean component on the stress history leads to lower durations.

- The failure mechanisms observed for constant amplitude tests at R=-1, R=0 and R=0.5 is similar to that observed for random tests. Instead, constant amplitude tests at R=$-\infty$ show remarkable differences.

- The random fatigue strength is well described by using the Miner's rule combined with the corrections for the mean stress effect. The values of the damage variable associated to the experiential tests are log-normally distributed, with a modal value equal to 1 and a standard deviation equal to the scatter of the S-N curve, in agreement with theoretical prediction.

- Although the scatter of the damage variable is coherent with the one of constant amplitude tests, we observed that the damage associated to random tests performed at the lowest value of RMS is slightly lower than one. These tests are associated to a damage evolution different from tests with similar duration performed at constant amplitude, as the presence of peak loads might modify the local damage propagation. The accuracy

of damage evolution description might be improved by using numerical models to study the local damaging mechanism, despite this requires significantly higher experimental and numerical efforts.

Acknowledgements

This research was done within the METAMatLab, a laboratory supported by Politecnico di Milano. The Italian Ministry of Education, University and Research is acknowledged for the support provided through the "Department of Excellence LIS4.0 - Lightweight and Smart Structures for Industry 4.0" Project. The important support given by BeamIT (Fornovo di Taro, PR, Italy) in providing the specimens is also acknowledge.

References

[1] L. J. Gibson and M. F. Ashby. *Cellular Solids*. Cambridge University Press, 1997.

[2] V. S. Deshpande, M. F. Ashby, and N. A. Fleck. Foam topology: Bending versus stretching dominated architectures. *Acta Mater.*, 49(6):1035–1040, 2001.

[3] V. S. Deshpande, N. A. Fleck, and M. F. Ashby. Effective properties of the octet-truss lattice material. *J. Mech. Phys. Solids*, 49:1747–1769, 2001.

[4] M. F. Ashby. The properties of foams and lattices. *Philos. Trans. R. Soc. A Math. Phys. Eng. Sci.*, 364:15–30, 2006.

[5] C Bonatti and D. Mohr. Large deformation response of additively-manufactured FCC metamaterials: From octet truss lattices towards continuous shell mesostructures. *Int. J. Plast.*, 92:122–147, 2017.

[6] T. Tancogne-Dejean, X. Li, M. Diamantopoulou, C. C. Roth, and D. Mohr. High Strain Rate Response of Additively-Manufactured Plate-Lattices: Experiments and Modeling. *J. Dyn. Behav. Mater.*, 5:361–375, 2019.

[7] S. Torquato, S. Hyun, and A. Donev. Optimal design of manufacturable three-dimensional composites with multifunctional characteristics. *J. Appl. Phys.*, 94:5748–5755, 2003.

[8] S. Torquato and A. Donev. Minimal surfaces and multifunctionality. *Proc. R. Soc. A Math. Phys. Eng. Sci.*, 460:1849–1856, 2004.

[9] F. S.L. Bobbert, K. Lietaert, A. A. Eftekhari, B. Pouran, S. M. Ahmadi, H. Weinans, and A. A. Zadpoor. Additively manufactured metallic porous biomaterials based on minimal surfaces: A unique combination of topological, mechanical, and mass transport properties. *Acta Biomater.*, 53:572–584, 2017.

[10] D. W. Abueidda, M. Elhebeary, C. S. Shiang, S. Pang, R. K. Abu Al-Rub, and I. M. Jasiuk. Mechanical properties of 3D printed polymeric Gyroid cellular structures: Experimental and finite element study. *Mater. Des.*, 165:107597, 2019.

[11] O. Al-Ketan and R. K. Abu Al-Rub. Multifunctional Mechanical Metamaterials Based on Triply Periodic Minimal Surface Lattices. *Adv. Eng. Mater.*, 21:1–39, 2019.

[12] M. G. Rashed, Mahmud Ashraf, R. A.W. Mines, and Paul J. Hazell. Metallic microlattice materials: A current state of the art on manufacturing, mechanical properties and applications. *Mater. Des.*, 95:518–533, 2016.

[13] S. Rajagopalan and R. A. Robb. Design and fabrication of biomorphic and durataxic tissue engineering scaffolds. *Med. Image Anal.*, 10:693–712, 2006.

[14] C. Yan, L. Hao, A. Hussein, and P. Young. Ti-6Al-4V triply periodic minimal surface structures for bone implants fabricated via selective laser melting. *J. Mech. Behav. Biomed. Mater.*, 51:61–73, 2015.

[15] S. Catchpole-Smith, R. R.J. Sélo, A. W. Davis, I. A. Ashcroft, C. J. Tuck, and A. Clare. Thermal conductivity of TPMS lattice structures manufactured via laser powder bed fusion. *Addit. Manuf.*, 30:100846, 2019.

[16] R.J. Sélo, S. Catchpole-Smith, I. Maskery, I. Ashcroft, and C. Tuck. On the thermal conductivity of AlSi10Mg and lattice structures made by laser powder bed fusion. *Addit. Manuf.*, 34:101214, 2020.

[17] W. Li, G. Yu, and Z. Yu. Bioinspired heat exchangers based on triply periodic minimal surfaces for supercritical CO2 cycles. *Appl. Therm. Eng.*, 179, 2020.

[18] R. Attarzadeh, M. Rovira, and C. Duwig. Design analysis of the 'Schwartz D' based heat exchanger: A numerical study. *Int. J. Heat Mass Transf.*, 177, 2021.

[19] I. Kaur and P. Singh. State-of-the-art in heat exchanger additive manufacturing. *Int. J. Heat Mass Transf.*, 178:121600, 2021.

[20] M. Benedetti, A. du Plessis, R. O. Ritchie, M. Dallago, S. M.J. Razavi, and F. Berto. Architected cellular materials: A review on their mechanical properties towards fatigue-tolerant design and fabrication. *Mater. Sci. Eng. R Reports*, 144:100606, 2021.

[21] G. Campoli, M. S. Borleffs, S. Amin Yavari, R. Wauthle, H. Weinans, and A. A. Zadpoor. Mechanical properties of open-cell metallic biomaterials manufactured using additive manufacturing. *Mater. Des.*, 49:957–965, 2013.

[22] S. Amin Yavari, R. Wauthle, J. Van Der Stok, A. C. Riemslag, M. Janssen, M. Mulier, J. P. Kruth, J. Schrooten, H. Weinans, and A. A. Zadpoor. Fatigue behavior of porous biomaterials manufactured using selective laser melting. *Mater. Sci. Eng. C*, 33:4849–4858, 2013.

[23] S. Amin Yavari, S. M. Ahmadi, R. Wauthle, B. Pouran, J. Schrooten, H. Weinans, and A. A. Zadpoor. Relationship between unit cell type and porosity and the fatigue behavior of selective laser melted meta-biomaterials. *J. Mech. Behav. Biomed. Mater.*, 43:91–100, 2015.

[24] M. Speirs, B. Van Hooreweder, J. Van Humbeeck, and J. P. Kruth. Fatigue behaviour of NiTi shape memory alloy scaffolds produced by SLM, a unit cell design comparison. *J. Mech. Behav. Biomed. Mater.*, 70, 2017.

[25] S. Zhao, S. J. Li, W. T. Hou, Y. L. Hao, R. Yang, and R. D.K. Misra. The influence of cell morphology on the compressive fatigue behavior of Ti-6Al-4V meshes fabricated by electron beam melting. *J. Mech. Behav. Biomed. Mater.*, 59:251–264, 2016.

[26] L. Huynh, J. Rotella, and M. D. Sangid. Fatigue behavior of IN718 microtrusses produced via additive manufacturing. *Mater. Des.*, 105:278–289, 2016.

[27] L. Boniotti, S. Foletti, S. Beretta, and L. Patriarca. Analysis of strain and stress concentrations in micro-lattice structures manufactured by SLM. *Rapid Prototyp. J.*, 26:370–380, 2020.

[28] L. Boniotti, S. Beretta, L. Patriarca, L. Rigoni, and S. Foletti. Experimental and numerical investigation on compressive fatigue strength of lattice structures of AlSi7Mg manufactured by SLM. *Int. J. Fatigue*, 128:105181, 2019.

[29] M. Dallago, S. Raghavendra, V. Luchin, G. Zappini, D. Pasini, and M. Benedetti. The role of node fillet, unit-cell size and strut orientation on the fatigue strength of Ti-6Al-4V lattice materials additively manufactured via laser powder bed fusion. *Int. J. Fatigue*, 142:105946, 2021.

[30] S. Leuders, M. Thöne, A. Riemer, T. Niendorf, T. Tröster, H.A. Richard, and H.J. Maier. On the mechanical behaviour of titanium alloy tial6v4 manufactured by selective laser melting: Fatigue resistance and crack growth performance. *International Journal of Fatigue*, 48:300–307, 2013.

[31] S. Beretta and S. Romano. A comparison of fatigue strength sensitivity to defects for materials manufactured by am or traditional processes. *International Journal of Fatigue*, 94:178–191, 2017. Fatigue and Fracture Behavior of Additive Manufactured Parts.

[32] P.D. Nezhadfar, R. Shrestha, N. Phan, and N. Shamsaei. Fatigue data for laser beam powder bed fused 17-4 ph stainless steel specimens in different heat treatment and surface roughness conditions. *Data in Brief*, 25:104215, 2019.

[33] P.D. Nezhadfar, R. Shrestha, N. Phan, and N. Shamsaei. Fatigue behavior of additively manufactured 17-4 ph stainless steel: Synergistic effects of surface roughness and heat treatment. *International Journal of Fatigue*, 124:188–204, 2019.

[34] T. Persenot, G. Martin, R. Dendievel, J.Y. Buffiére, and E. Maire. Enhancing the tensile properties of ebm as-built thin parts: Effect of hip and chemical etching. *Materials Characterization*, 143:82–93, 2018.

[35] T. Persenot, A. Burr, E. Plancher, J.Y. Buffière, R. Dendievel, and G. Martin. Effect of ultrasonic shot peening on the surface defects of thin struts built by electron beam melting: Consequences on fatigue resistance. *Additive Manufacturing*, 28:821–830, 2019.

[36] T. Persenot, A. Burr, R. Dendievel, J.Y. Buffière, E. Maire, J. Lachambre, and G. Martin. Fatigue performances of chemically etched thin struts built by selective electron beam melting: Experiments and predictions. *Materialia*, 9:100589, 2020.

[37] J. de Krijger, C. Rans, B. Van Hooreweder, K. Lietaert, B. Pouran, and A. A. Zadpoor. Effects of applied stress ratio on the fatigue behavior of additively manufactured porous biomaterials under compressive loading. *J. Mech. Behav. Biomed. Mater.*, 70:7–16, 2017.

[38] K. Lietaert, A. Cutolo, D. Boey, and B. Van Hooreweder. Fatigue life of additively manufactured Ti6Al4V scaffolds under tension-tension, tension-compression and compression-compression fatigue load. *Sci. Rep.*, 8, 2018.

[39] L. Boniotti, S. Dancette, M. Gavazzoni, J. Lachambre, J.Y. Buffiere, and S. Foletti. Experimental and numerical investigation on fatigue damage in micro-lattice materials by digital volume correlation and μct-based finite element models. *Engineering Fracture Mechanics*, 266:108370, 2022.

[40] C. M. Styles, S. L. Evans, and P. J. Gregson. Development of fatigue lifetime predictive test methods for hip implants: Part I. Test methodology. *Biomaterials*, 19, 1998.

[41] H. L. Ploeg, M. Bürgi, and U. P. Wyss. Hip stem fatigue test prediction. *Int. J. Fatigue*, pages 894–905, 2009.

[42] S. L. Evans. Effects of intermittent overloads on fatigue of PMMA bone cement. *Int. J. Nano Biomater.*, 3:65–77, 2010.

[43] P. C Mckeighan. *Fatigue Testing and Analysis under Variable Amplitude Loading Conditions*. Number 1439. 2003.

[44] European Commitee for Standardization. *Eurocode 9: Design of aluminium structures - Part 1-3: Structures susceptible to fatigue*. 2009.

[45] M. Gavazzoni, M. Pisati, S. Beretta, and S. Foletti. Multiaxial static strength of a 3D printed metallic lattice structure exhibiting brittle behavior. *Fatigue Fract. Eng. Mater. Struct.*, 44:3499–3516, 2021.

[46] American Society for Testing and Materials. *E739 - Standard Practice for Statistical Analysis of Linear or Linearized Stress-Life (S-N) and Strain-Life Fatigue Data*. 2015.

[47] International Organization for Standardization. *ISO 12107 - Metallis materials - Fatigue testing - Statistical planning and analysis of data*. 2011.

[48] M.F. Ashby, A. Evans, N.A. Fleck, L.J. Gibson, J.W. Hutchinson, and H.N.G. Wadley. Metal foams: A design guide. *Applied Mechanics Reviews*, 54:B105–B106, 2001.

[49] Y. Sugimura, A. Rabiei, A.G. Evans, A.M. Harte, and N.A. Fleck. Compression fatigue of a cellular al alloy. *Materials Science and Engineering: A*, 269:38–48, 1999.

[50] S.J. Li, L.E. Murr, X.Y. Cheng, Z.B. Zhang, Y.L. Hao, R. Yang, F. Medina, and R.B. Wicker. Compression fatigue behavior of ti–6al–4v mesh arrays fabricated by electron beam melting. *Acta Materialia*, 60:793–802, 2012.

[51] Y.J. Liu, H.L. Wang, S.J. Li, S.G. Wang, W.J. Wang, W.T. Hou, Y.L. Hao, R. Yang, and L.C. Zhang. Compressive and fatigue behavior of beta-type titanium porous structures fabricated by electron beam melting. *Acta Materialia*, 126:58–66, 2017.

[52] M. Pisati, M. G. Corneo, S. Beretta, S. Foletti, E. Riva, and F. Braghin. Numerical and Experimental Investigation of Cumulative Fatigue Damage under Random Dynamic Cyclic Loads of Lattice Structures Manufactured by Laser Powder Bed Fusion. *Metals*, (11):1395, 2021.

[53] American Society for Testing and Materials. *E1049 - Standard practices for cycle counting in fatigue analysis*. 2017.

[54] D. Taylor. *The Theory of Critical Distances*. Elsevier, United States, 2007.

[55] S. Beretta, M. Gargourimotlagh, S. Foletti, A. du Plessis, and M. Riccio. Fatigue strength assessment of "as built" alsi10mg manufactured by slm with different build orientations. *International Journal of Fatigue*, 139:105737, 2020.

[56] C. Berger, K. G. Eulitz, P. Heuler, K. L. Kotte, H. Naundorf, W. Schuetz, C. M. Sonsino, A. Wimmer, and H. Zenner. Betriebsfestigkeit in Germany - An overview. *Int. J. Fatigue*, 24:603–625, 2002.

[57] E Haibach. *Betriebsfestigkeit [Structural durability]*. VDI-Verlag, 2nd edition, 2002.

[58] P. H. Wirsching and M. C. Light. Fatigue under wide band random stresses. *Journal of the Structural Divsion of American Society of Civil Engineers*, 106:1265–1278.

[59] W. H. Munse, T. W. Wilbur, M. L. Tellalian, K. Nicoll, and K. Wilson. Fatigue characterization of fabricated ship: Details for design, report–318, 1983.

[60] C. Sundararajan. *Probabilistic Structural Mechanics Handbook – Theory and Industrial Applications*. Springer, 1995.

Declaration of interests

☒ The authors declare that they have no known competing financial interests or personal relationships that could have appeared to influence the work reported in this paper.

☐The authors declare the following financial interests/personal relationships which may be considered as potential competing interests: